Payload characterization for CubeSat demonstration of MEMS deformable mirrors

Anne Marinan*[a], Kerri Cahoy[a,b], Matthew Webber[b], Ruslan Belikov[c], Eduardo Bendek[c]

[a]Dept. of Aeronautics and Astronautics, Massachusetts Institute of Technology, 77 Massachusetts Avenue, Cambridge, MA, USA 01239; [b]Dept. of Earth, Atmospheric, and Planetary Sciences, Massachusetts Institute of Technology, 77 Massachusetts Avenue, Cambridge, MA, USA 01239; [c]NASA Ames Research Center, Moffett Blvd, Moffett Field, CA 94039

ABSTRACT

Coronagraphic space telescopes require wavefront control systems for high-contrast imaging applications such as exoplanet direct imaging. High-actuator-count MEMS deformable mirrors (DM) are a key element of these wavefront control systems yet have not been flown in space long enough to characterize their on-orbit performance. The MEMS Deformable Mirror CubeSat Testbed is a conceptual nanosatellite demonstration of MEMS DM and wavefront sensing technology. The testbed platform is a 3U CubeSat bus. Of the 10 x 10 x 34.05 cm (3U) available volume, a 10 x 10 x 15 cm space is reserved for the optical payload. The main purpose of the payload is to characterize and calibrate the on-orbit performance of a MEMS deformable mirror over an extended period of time (months). Its design incorporates both a Shack Hartmann wavefront sensor (internal laser illumination), and a focal plane sensor (used with an external aperture to image bright stars). We baseline a 32-actuator Boston Micromachines Mini deformable mirror for this mission, though the design is flexible and can be applied to mirrors from other vendors. We present the mission design and payload architecture and discuss experiment design, requirements, and performance simulations.

Keywords: MEMS Deformable Mirrors, Adaptive Optics, Wavefront Sensing, CubeSat

1. INTRODUCTION

Adaptive optics will play a crucial role in future space-based observation and communications missions. High-actuator count microelectromechanical systems (MEMS) deformable mirrors are key elements in these adaptive optics systems. While these mirrors have been successfully demonstrated in many ground-based applications, they have not been qualified nor had their performance characterized for long-duration space operations. Efforts are currently underway to perform vibration, thermal, and radiation characterization, but extended in situ demonstration is required to fully understand and characterize the behavior of these devices on orbit to enable integration of these deformable mirrors into high-contrast imaging on space telescopes.

The Deformable Mirror Demonstration Mission (DeMi) is a nanosatellite that will serve as an on-orbit testbed for a MEMS deformable mirror. The mirror baselined for demonstration is a Boston Micromachines Mini (32-actuator) mirror. The mission is in the conceptual design phase. This work presents the operational and experimental concepts of the mission as well as performance requirements and simulations for the optical payload.

1.1 Motivation

Applications for wavefront control systems in space can be grouped into four general categories: (i) systems that take images through the Earth's turbulent atmosphere, (ii) systems that transmit and receive laser signals through the Earth's turbulent atmosphere, (iii) systems that take high contrast and high dynamic range images of other objects in space, or (iv) systems that transmit laser signals to and receive laser signals from other objects in space. Deformable mirrors are a key technology needed to perform the optical corrections in wavefront control systems, including high contrast imaging of exoplanets with space telescopes and space-based free space optical laser communications.

In order to image an Earth-like planet, an exoplanet direct imaging system needs to achieve a contrast ratio of 1×10^{-10}. Even with adaptive optics on a large ground-based telescope, it is currently not possible to overcome the effects from

*marinana@mit.edu

atmospheric turbulence to achieve the high contrast needed to obtain high-resolution spectra of an Earth-like exoplanet[2,3,4]. While a space telescope does not have to overcome the effects of atmospheric turbulence, it is usually at the expense of smaller aperture size (e.g., due to launch cost and launch vehicle limitations). The performance of a space telescope will still suffer from optical imperfections, thermal distortions, and diffraction that will corrupt the wavefront, create speckles (see Figure 1), and ruin the contrast[5,6,7].

The spatial frequency of aberrations in the pupil plane determines where the speckles caused by these aberrations will land in the focal plane. The speckles represent the spatial Fourier transform of these periodic disturbances in the image plane[8], so the higher the spatial frequency of the aberration, the further off-axis the speckle will land in the focal plane. High actuator count deformable mirrors have the authority to correct high spatial frequency aberrations that would otherwise degrade the contrast in these locations[9,10].
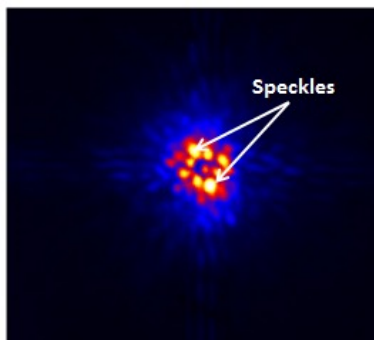

Figure 1: Speckles from atmospheric turbulence and telescope imperfections are clear in this image of 55 Cancri taken with the Lyot Project coronagraph on the Air Force Advanced Electro Optical System (AEOS) Telescope[11]

1.2 Space Qualification of MEMS DMs

Ground-based testbeds are used to develop methods for wavefront sensing and mirror control to improve the quality and approach of space-based imaging with active optics systems. Space-qualified components must survive launch (extreme vibration and acoustic environment) as well as continued operation in space (microgravity, vacuum, radiation, thermal considerations). There are ground-based tests that can be performed to demonstrate a component's capability including thermal vacuum testing, vibration testing, acoustic testing, and total ionizing dose and single event radiation testing. Some testing, however, such as microgravity and in-situ operation, require flight demonstration.

The Ames Coronagraph Experiment (ACE) facility develops and tests new methods and technology for exoplanet imaging[12]. The tests can be run in both non-stabilized and temperature-stabilized air. The test facility is depicted in Figure 2. This platform is used to test the payload for the Exoplanetary circumstellar environments and disk explorer (EXCEDE) mission, a future space telescope that baselines a phase-induced amplitude apodization (PIAA) coronagraph and 2000-actuator Boston Micromachines Corporation (BMC) MEMS deformable mirror[13].
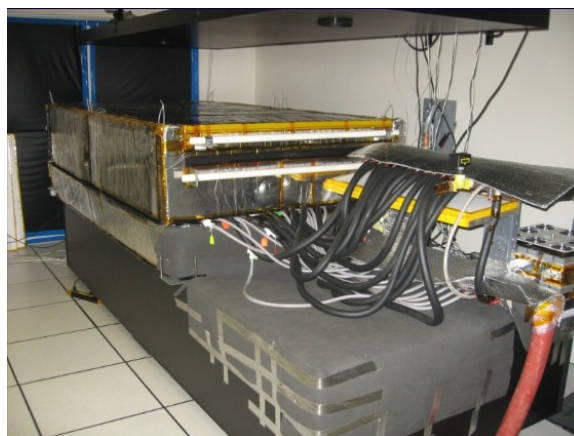

Figure 2: The Ames Coronagraph Experiment (ACE) testbed is a temperature-stabilized facility for testing new coronagraphic technologies[14]

The Jet Propulsion Laboratory also has a testbed for coronagraph optical systems and components: the High-Contrast Imaging Testbed (HCIT). The optical table is enclosed in a thermally controlled vacuum tank, providing isolation from vibration and turbulence[15]. This setup is depicted in Figure 3.
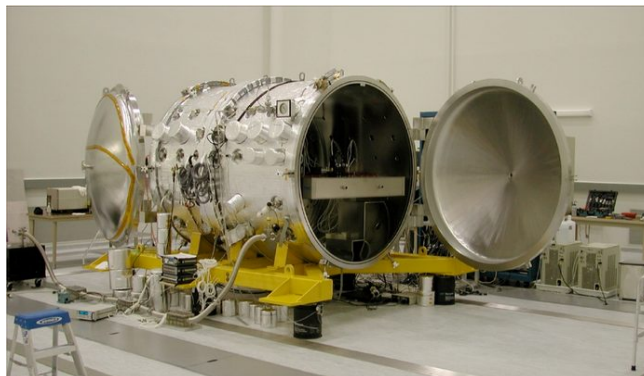

Figure 3: The High Contrast Imaging Testbed at JPL enables testing of coronagraph systems in a vacuum environment[16].

There are several space-based missions that have demonstrated or are planned to demonstrate the use of deformable mirrors and adaptive optics in space, such as Boston University's PICTURE (Planet Imaging Concept Testbed Using a Rocket Experiment)[17]. The first iteration of this experiment experienced a telemetry failure, but PICTURE-2 is undergoing construction and testing for a late 2014 flight.

Other relevant space-based efforts include the South Korean MEMS Telescope for Extreme Lightning (MTEL)[18,19] and the James Webb Space Telescope microshutter array[20], though the actuators and functionality of the mirrors on these missions are very different from the MEMS DMs required for high contrast imaging.

1.3 CubeSat Platform

A CubeSat is a nanosatellite with strict standards for size, mass, power, and launch configurations. The CubeSat standard was developed by the California Polytechnic Institute to encourage a platform with a consistent launch vehicle interface that would enable interested parties, mainly universities, to build low-cost satellites for science missions. COTS (Commercial Off-the-Shelf) components are an integral part of CubeSat design, and there are companies that tailor components and structures specifically to CubeSat needs (Pumpkin, Clyde Space, etc.). They are relatively cheap and simple to produce as compared with components and systems for larger satellites. Each unit (U) of a CubeSat is a 10 x 10 x 10 cm cube with a mass of 1.33 kg[21]. CubeSat deployers and the standards to which each CubeSat is designed were developed to ensure the consistency of these secondary payloads and to minimize risk to the primary mission.

CubeSats are increasingly viable platforms for scientific applications[22,23,24,25] and technology demonstrations. One of the challenges with doing this optical demonstration on a CubeSat is the available pointing control authority on such a constrained system. This is an active area of research[26,27]. Launch opportunities are available fairly frequently for these secondary payloads[28], and programs such as the NASA Educational Launch of Nanosatellites (ELaNa) offer secondary launch opportunities at minimal cost to qualifying missions at educational institutions.

2. MISSION DESIGN

2.1 Mission Goals

The main goal of the CubeSat Deformable Mirror Demonstration is to raise the technology readiness level (TRL) of a BMC Mini (32-actuator) Deformable Mirror to TRL 7. In order to successfully demonstrate this, the mission objectives are to verify the performance of the mirror over long-duration operation in orbit (relevant environment) and in closed loop wavefront correction with both an internal and an external source. This mission will not perform any high-contrast imaging; rather, it is a demonstration of the technology required to accomplish this capability on future space-based platforms.

The performance objective is to demonstrate a closed loop wavefront correction system capable of correcting a wavefront to $\lambda/100$. The mirror performance is determined based on the observed mirror response to a sequence of predetermined sequence of actuations. Successful demonstration is determined based on the ability of the mirror to

correct an image or a signal using closed-loop control. The expected behavior of the mirror is determined through hardware experimentation as well as optical modeling.

2.2 Operational Overview

The CubeSat will be launched into a low-earth orbit as a secondary payload. The baseline orbit design for this mission is 415 km altitude, 52-degree inclination. From this orbit the satellite will have an expected operational lifetime of approximately 4 months.

There are two modes of operation for the satellite experiments: mirror characterization with an internal source, and observation and image correction of a bright star through an external aperture. For the first part of the mission, an internal laser illuminates the mirror to characterize the performance of the deformable mirror through open-loop actuator deflection measurement and closed loop correction with a Shack-Hartmann wavefront sensor. Once the mirror has been characterized, the telescope will target bright stars and use the deformable mirror for closed-loop image correction based on the quality of the focal plane image. The intended targets for star imaging are Vega, Alpha Centauri, Arcturis, Sirius, and Canopus. The external observation requires much finer pointing and stability control than the internal laser experiment.

The intended experiments are defined based on the source and detector used, as summarized in Table 1. Section 3 provides details of the internal laser experiments, and Section 4 explains the external star imaging experiment.

Table 1: Optical payload experiment summary

Experiment #	Source	Sensor	Purpose
0	Internal Laser source	Shack-Hartmann	Open and closed loop mirror characterization
1	Internal Laser source	Focal plane	Closed loop wavefront sensing and correction demonstration
2	External source	Focal plane	Closed loop imaging, wavefront sensing and correction demonstration

2.3 System Design

The overall spacecraft platform is a 3U CubeSat, with 1.5U allocated to the optical payload and 1.5U to the supporting bus and interface. Figure 4 shows an isometric view of this design.
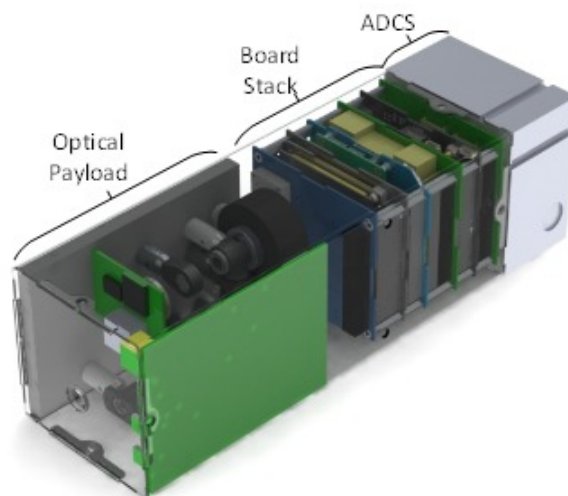

Figure 4: 3U DeMi CubeSat (with transparent walls). The 1.5U optical payload includes an internal illumination source as well as a ½-inch aperture to image external objects.

The design of the supporting bus is based on the components from the Microsized Microwave Atmospheric Satellite (MicroMAS)[29], a 3U CubeSat designed and built by the MIT Space Systems Laboratory and MIT Lincoln Laboratory for a mid-2014 launch. The structure is custom-designed to accommodate cutouts, the payload, and interfaces with bus components. The power system consists of externally-mounted solar panels, a secondary battery, and electrical power system from Clyde Space. The satellite will communicate in the UHF range using a deployed monopole tape-spring antenna (not pictured) and Cadet radio from L3-Communications. Three-axis attitude determination and control is required to point at a star, and the baseline system is an MAI400 from Maryland Aerospace, Incorporated. The MAI400 includes three orthogonally-mounted reaction wheels, three orthogonally-mounted torque rods, and two Earth horizon sensors. Additional attitude sensors include sun sensors, an inertial measurement unit, and a magnetometer. The main processor will either be a microprocessor or an FPGA, and custom circuitry will be designed for interfaces with payload electronics.

2.4 Payload Design

The volume allocated for the optical payload is 150 x 95 x 95 mm volume, with 150 x 95 x 25 mm for the mirror driver electronics and 150 x 95 x 70 mm for the optical system. The intended layout for the system is shown in Figure 5.
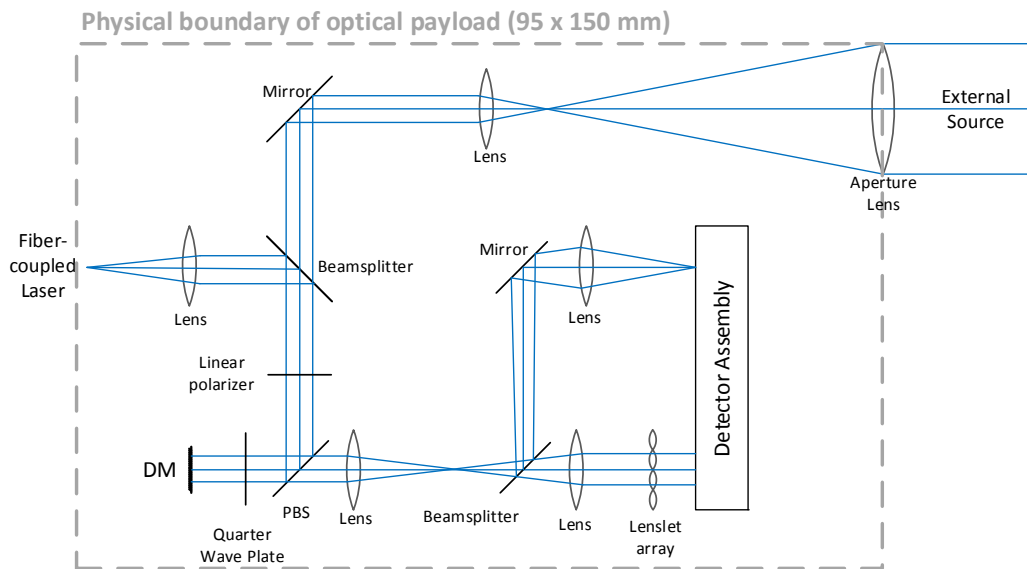

Figure 5: Optical payload layout. Dashed line indicates physical boundary (150 mm x 95 mm). The detector assembly holds two detectors – one for the focal plane sensor (upper) and one for the Shack-Hartmann sensor (lower).

The system accommodates two sources: an internal fiber-coupled laser and an external source (bright star). A nonpolarizing beamsplitter is used as a combiner to put the internal and external source on the same optical path. The beam encounters a linear polarizer and is polarized such that it reflects off of the polarizing beamsplitter, passes through a quarter wave plate, and is perpendicularly incident on the deformable mirror. When the beam reflects and again passes through the quarter wave plate, the polarization is rotated 90 degrees such that the beam transmits through the polarizing beamsplitter. From there, a third beamsplitter divides the beam so a portion goes to the Shack-Hartmann sensor and the rest is focused down to a detector.

Two separate detectors are used for the Shack Hartmann and focal plane sensor, although they are integrated on a single board (as depicted in Figures 5, 6, 11, and 13) to simplify electronics wiring and interfaces. Due to the physical size of the optics in the system, the sensors cannot both be imaged on a single off-the-shelf detector. The experiments are designed such that the detectors never operate simultaneously.

2.5 Baseline components

Wherever possible, commercial off-the-shelf (COTS) components are considered for the payload.

The mirror chosen for demonstration is the Boston Micromachines (BMC) Mini DM (32 actuators). A 64 x 64 array with the same technology from this manufacturer is currently used on the Gemini Planet Imager (GPI), and a 2000-actuator

mirror (also from BMC) is planned for use in the EXoplanetary Circumstellar Environments and Disk Explorer (EXCEDE) mission. Table 2 gives operational parameters of the "mini" as compared to the "kilo." There are several other deformable mirror manufacturers that we are considering as well, such as Xinetics and Iris AO. The constrained volume for the driver is the primary motivation behind using the mini mirror. There is work on developing more compact application-specific integrated circuit (ASIC) drivers, which would enable demonstration of a mirror with more actuators on this platform.[30]

Table 2: Boston Micromachines MEMS Deformable Mirror Parameters

Parameter	Mini (6x6) 5 μm stroke	Mini (6x6) 1.5 μm stroke	Kilo 1.5 μm stroke
# Actuators	32	32	1020 (square) 952 (circle)
Aperture (mm)	2.25	1.5	9.3
Pitch (μm)	450	300	300
Mechanical response time (μs)	<500	<20	<20
Inter-actuator coupling	22%	15%	15% (+/- 5%)
Surface finish (nm rms)	<30	<30	<30
Driver dimensions (in)	4 x 5.25 x 1.2	4 x 5.25 x 1.2	5.23 x 19 x 14

The detectors are both Aptina MT9P031 monochromatic detectors with 2.2 um pixel pitch. Currently the fiber-coupled laser and other optical components are based on available COTS components from Thorlabs and Newport. In order to fit within the constrained volume, custom optical mounts and a custom electronics board that incorporates both detectors are required. The main structure of the payload will be 3D printed to minimize thermal mismatch and mechanical misalignments between optical components.

3. INTERNAL SOURCE EXPERIMENT

Mirror characterization with the internal source includes experiments utilizing each of the Shack-Hartmann wavefront sensor and the focal plane image. An open-loop experiment with the Shack Hartmann sensor serves to verify the deflections of the mirror actuators, and separate closed-loop experiments with the Shack Hartmann sensor and focal plane array validate the performance of the mirror with two image correction techniques.

3.1 Experiment 0: Internal Source with Shack-Hartmann sensor

The Shack-Hartmann sensor is only used with the internal source. The Shack-Hartmann sensor measures the wavefront reflected off the mirror in order to verify open-loop commanded actuations. The sensor is also used to verify the operation of the mirror in performing closed-loop wavefront correction.

3.1.1 Optical path

The optical path used for this experiment has the least common path with the external source focal plane image, but the purpose of this configuration is just to characterize the mirror operation. Figure 6 shows the beam path through the optical components for this payload architecture.
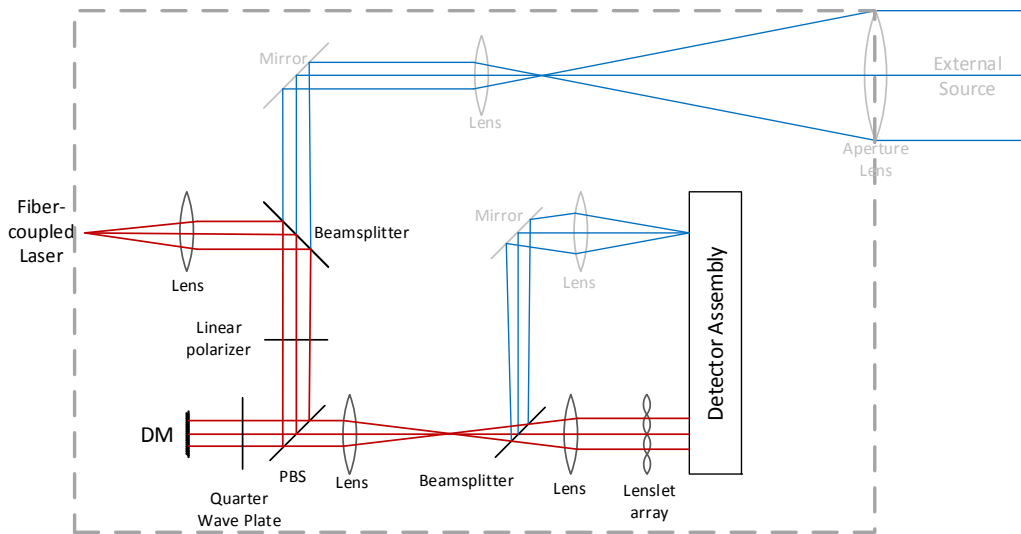
Figure 6: Beam path (red) from the internal fiber-coupled laser to the detector of the Shack-Hartmann sensor

For mirror characterization, the mirror is commanded to a predetermined series of surface maps that include individual actuator pokes as well as low-order Zernike functions. The internal laser is used as the illumination source, and a Shack-Hartmann wavefront sensor onboard generates spot field images of each mirror deflection.

3.1.2 Experiment 0 description

There are two modes of operation for this experiment: open-loop and closed loop. In open-loop mode, the mirror will be commanded to a predetermined series of actuator patterns (individual actuator pokes as well as Zernike modes to different levels of mirror stroke). For each mirror actuation, vectors of x and y displacements of each spot centroid are sent to the ground. Communications data rate permitting, the spot field images will also be downlinked. On the ground, the wavefronts will be reconstructed to evaluate and verify the correctness of the mirror shape. Figure 7 offers a functional flow diagram of this experiment.
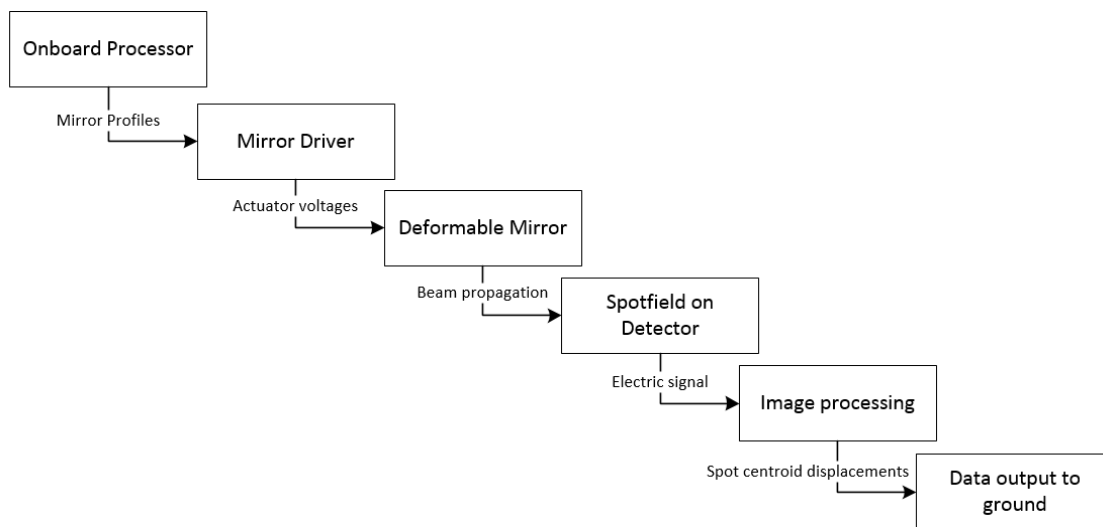

Figure 7: Open-loop mirror characterization with wavefront sensor

To ensure experiment success, the sensor must be able to measure the mirror surface displacement to the maximum mirror stroke (up to 11 μm) with a resolution of less than 10 nm. The success criteria on the mirror are that the measured actuator deflections are within 10 nm of the commanded deflections and that these tests are 95% repeatable over the mission lifetime.

For closed-loop operation, the centroid offsets for each lenslet are fed back into the onboard processor where an algorithm determines the proper mirror actuation to minimize the centroid displacement. The data products sent to the ground include the final centroid displacements, the final mirror command, and the focal plane image before and after wavefront correction. Figure 8 illustrates the flow of operation and information.
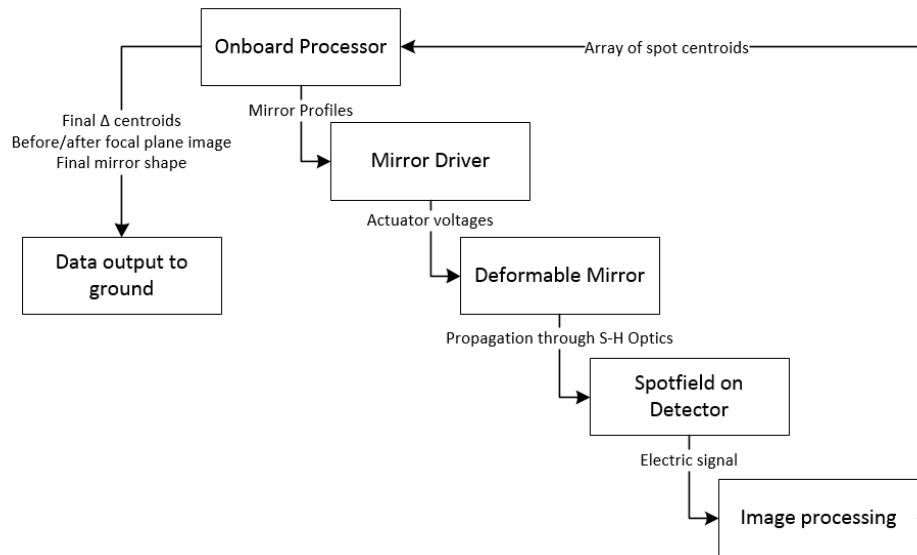

Figure 8: Closed-loop mirror characterization with wavefront sensor

The success criteria for the closed-loop control are that the algorithm converges on correction to a final surface wavefront error of less than 10 nm rms in one minute and that the actuators stay within 10%-90% of the stroke range.

3.1.3 Baseline Design Parameters

The BMC mini mirror has a continuous gold facesheet with piston-only actuators. The wavefront sensor is designed such that the lenslets are aligned with the corners of the mirror actuators as illustrated in Figure 9.
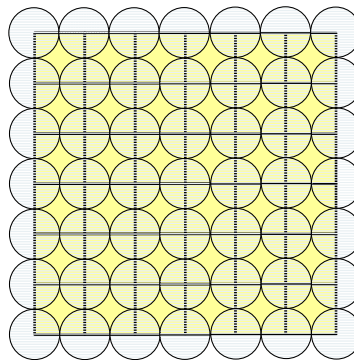

Figure 9: The lenslets (blue) in the Shack Hartmann sensor are aligned with the corners between mirror actuators (yellow)

Selection of the lenslet parameters is driven by the desired spot sampling and dynamic range for the detector[31]. The spots should be close to critically sampled. On the detector, each lenslet aperture is assigned a grid of pixels. The wavefront tilt across the lenslet can be measured unambiguously as long as the spot is contained within its grid. In order to completely characterize the mirror, the Shack Hartmann sensor should be able to detect the maximum mirror stroke – for the largest available mirror stroke (5.5 µm) this corresponds to a total surface wavefront error of 11 µm.

The resolution of the measurement is limited by the overall uncertainty in the centroid position measurement. The desired measurement resolution is $\lambda/100$, or ~6 nm at the design wavelength. The corresponding displacement on the detector depends on the geometry of the lenslet and detector and dictates the maximum allowable centroid displacement error. The centroid measurement error is primarily a function of the signal-to-noise ratio at the detector[30] – because the

source is a laser, the photon count can be adjusted to minimize this error. A detailed analysis of the design and implementation of the centroiding algorithm and resulting error is an area of future work for the optical system design.

Once given the requirements on spot sampling, maximum detectable wavefront error, and desired resolution, then the lenslet and detector designs can be calculated. We limited the detector geometry to commercially-available components. Aptina manufactures detectors with varying pixel sizes, but the two detectors of most interest had pixel pitches of 2.2 and 5.2 μm. From these two detector options we calculated the ideal lenslet focal length and pitch for the system. These results were compared with off-the-shelf lenslets from Newport, Thorlabs, and Edmund Optics. The calculations were repeated for the lenslet arrays that most closely matched the ideal parameters. These results are summarized in Table 3.

Table 3: Baseline design for the Shack-Hartmann wavefront sensor (chosen design in italics)

Category	Parameter	Ideal 2.2 um	*Physical 2.2 um*	Ideal 5.2 um	Physical 5.2 um	Units
Given component metrics	Pixel diameter	2.2	*2.2*	5.2	5.2	μm
	Lenslet pitch	230	*300*	540	500	μm
	Lenslet focal length	2.0	*4.8*	11.4	13.8	mm
Calculated metrics	Spot sampling	3.0	*4.6*	3.0	3.4	pixels/ (λ/D)
	Number of pixels across lenslet	104	*136*	104	96	pixels
	Total pixels across spotfield	728	*955*	728	673	pixels
Calculated performance	Maximum detectable wf error	11	*12*	11	7	μm
	Centroid error for desired resolution	0.026	*0.046*	0.026	0.034	pixels

The 2.2 μm-pixel detector with 300 μm lenslets was chosen based on the detectable range and the slightly more lenient allowable centroid error.

One of the aspects of the mirror characterization experiment involves putting Zernike functions across the mirror and measuring the resulting spot displacements. Figure 10 shows the nominal positions of the centroids and the displaced spots from an input wavefront with 2 μm peak-to-peak astigmatism. The image is of the detector plane and reflects the design parameters of the system as defined above.
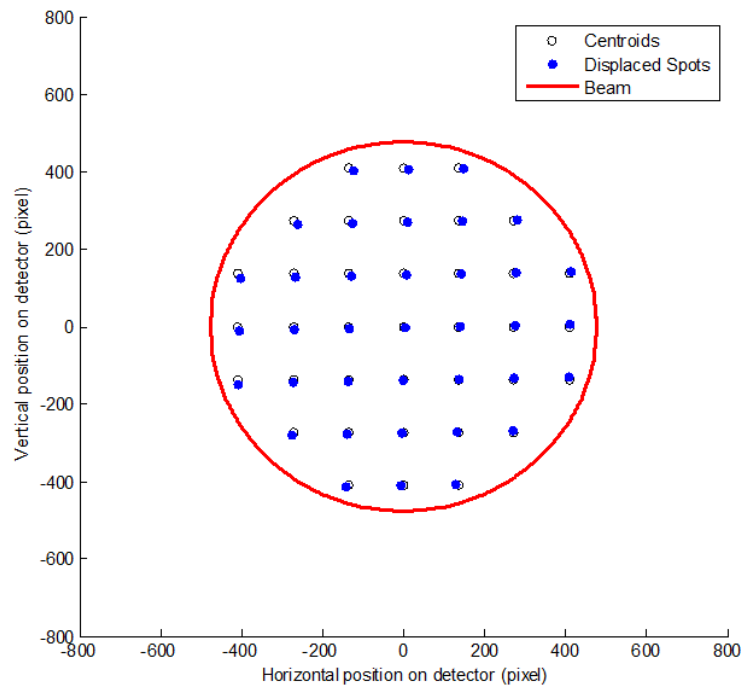

Figure 10: Simulated spot field with 2 μm peak-to-peak astigmatism wavefront error

The goal of this simulation is to generate the expected spotfields for each of the intended mirror deflections – both individual actuator deflections and low-order Zernike mode surfaces. In future implementations, a wavefront sensing algorithm will find the centroid deviations, generate the wavefront at the lenslet array, and calculate the shape of the mirror. This algorithm will be tested on a laboratory hardware setup.

3.2 Experiment 1: Internal source with focal plane sensor

The internal source is also used to perform closed-loop wavefront correction with the focal plane sensor. The primary contributions of wavefront error are expected to be defocus, astigmatism, and coma from the effects of fast optics, small optical misalignments, and thermal gradients across the payload.

3.2.1 Optical path

The optical path for this experiment uses the focal plane image rather than the Shack-Hartmann, eliminating the non-common path errors with the external source downstream of the mirror. The beam path through the system is illustrated in Figure 11. Section 4.2 goes into more detail on the optical parameters of the focal plane sensor.
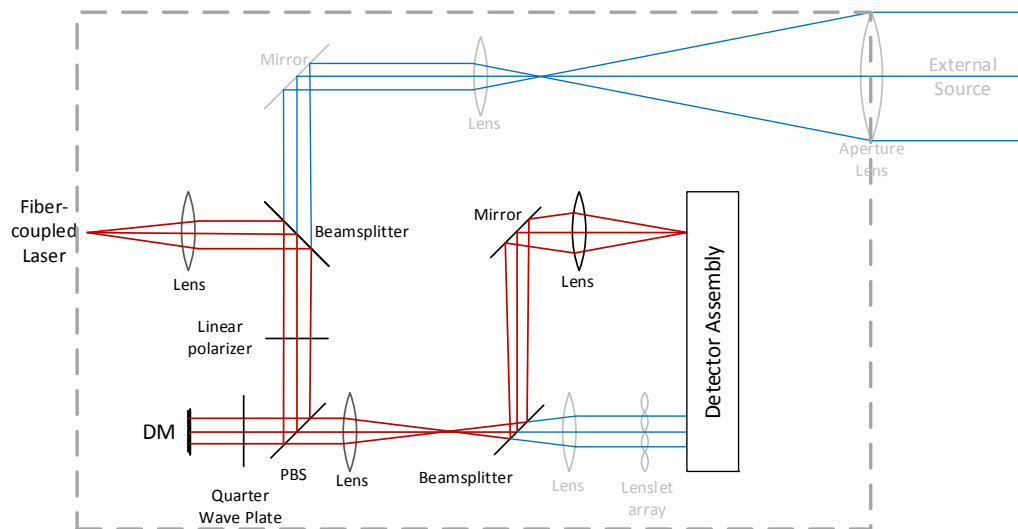

Figure 11: Beam path (red) from the internal fiber-coupled laser to the focal plane detector

3.2.2 Experiment 1 description

The closed-loop correction with the focal plane sensor is accomplished using a hill-climb diversity approach. Each Zernike mode (focus, coma, and astigmatism) will be applied to the mirror in varying magnitude and orientation with the resulting Strehl number calculated for each mirror actuation. The actuations that maximize the Strehl number for each mode will be superimposed on each other to create the final mirror actuation and generate a corrected image. Figure 12 shows the flow of information through the closed loop and to the ground.
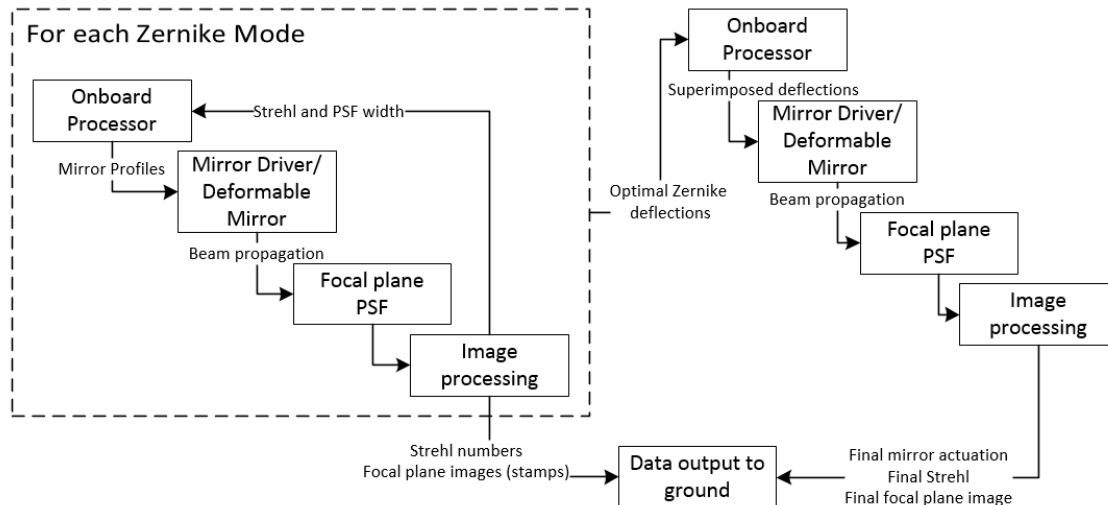
Figure 12: Closed-loop mirror characterization with focal plane image

The data downlinked to the ground include the calculated Strehls and point spread function (PSF) image during correction, the pre- and post-correction focal plane images, and the final array of commanded mirror actuations. The goal is to correct the final image to a Strehl of 0.85 over the course of one minute with the mirror actuators staying within 10-90% of the actuation stroke.

4. EXTERNAL SOURCE EXPERIMENT

Experiment 2 uses the external source (bright star) with the focal plane detector. For high-contrast imaging space telescopes, the source of illumination in the system is a star or other external source; thus, in this mission, an external aperture allows the optical payload telescope to observe a bright star and verify mirror operation. Over the course of the observation, one of two wavefront correction options will be used: open-loop using the final mirror shape based on correction using the internal source or closed-loop using the hill-climbing focal plane wavefront correction described in section 3.2.2.

4.1 Optical path

The beam path for this experiment utilizes the external source and creates a corrective telescope in the optical payload. Figure 13 illustrates the beam path through the system. The main difference between this and the internal source architecture are the optical components upstream of the beam combiner. The expected main contributions of wavefront error are tip/tilt, defocus, astigmatism, and coma from optical misalignments, thermal distortion, and spacecraft jitter.
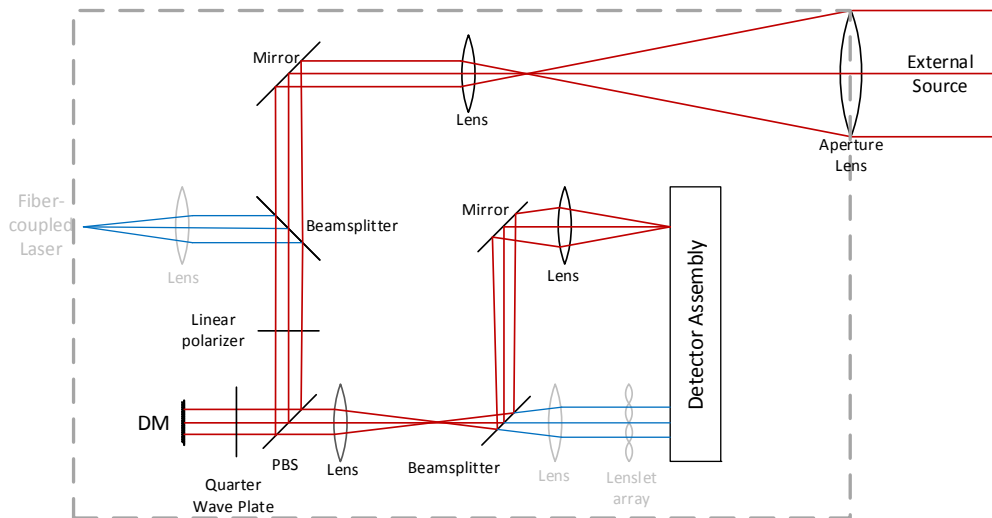
Figure 13: Beam path (red) from the external source to the focal plane detector

4.2 Experiment 2 Description

Both open-loop and closed-loop wavefront correction will be done with the internal source using the focal plane sensor. In the open-loop correction, the final mirror actuation from closed-loop correction with the internal source will be applied to the mirror. This will remove aberrations from elements in the common path with the internal source. The focal plane image and Strehl number before and after mirror actuation will be recorded and sent to the ground.

Closed-loop control, using the same hill-climb approach as with the internal source (see Section 3.2.2), will then correct for non-common path errors upstream of the deformable mirror. The requirements on correction for this experiment are less stringent than with the internal source due to the added complication of spacecraft pointing. The success criterion for the closed-loop experiment is to correct the final image to a Strehl of 0.80 over the course of the star observation with the mirror actuators staying within 10-90% of the stroke range.

4.3 Baseline Design Parameters

The focal telescope is designed for the external source. The goal for this design is again to optimize the system performance within the limitations of readily-available components. The detector for the focal plane image is the same as for the Shack-Hartmann sensor – 2.2 µm-pixel Aptina MT9P031 – to minimize complexity with the detector interface.

A few initial design decisions drove the rest of the optical layout for the telescope: the observation wavelength, overall architecture, and detector. From these top-level decisions, we calculated more specific requirements on the optical system and determined the minimum brightness for the target star. Table 4 summarizes these parameters.

These calculations were made based on the maximum frame rate of the detector. With the shortest possible exposure time, stars brighter than magnitude 0.6 can be imaged with this system. The short exposure time was primarily driven by the desire to minimize the effects of jitter and spacecraft instability on the observations.

Observing a bright star requires the spacecraft to be stably pointed to (a) ensure that the observation time of the object is sufficient to carry out the intended experiment (low frequency drift) and (b) minimize the movement of the image on the detector over the integration time required for each readout (high frequency jitter). Section 4.4 goes into more detail on the feasibility of star observations and the requirements on platform stability.

Table 4: Baseline design for the focal plane telescope

Category	Parameter	Threshold	Units
Chosen	Observation wavelength range	400 – 700	nm
	Aperture Diameter	12.7	mm
	System throughput	10	%
	Detector quantum efficiency	55	%
	Detector pixel pitch (one dimension)	2.20	μm
	Detector size	2592 x 1944	pixels
	Detector maximum readout rate	53	frames/s
	Desired spot sampling	3	pixels/(λ/D)
	Reference star (Vega) photon flux	1.37E+26	photons/m^2/s/sr
Calculated	Minimum exposure time	0.019	s
	System resolution (1.22 L/D)	10.9	as
	Detector Plate Scale	2.98	as/pixel
	Telescope Effective Focal Length	152	mm
	Telescope F#	12	--
	Telescope Field of View (width)	2.1	degrees
	Telescope Field of View (height)	1.6	degrees
Performance	Required star magnitude for SNR 10	0.61	--

4.4 Bright star observations

Figure 14 shows a plot of the simulated accesses for this spacecraft assuming a spacecraft slew rate of 0.1 degrees/s with a 1.6 x 2.1 degree field of view. Over the course of one year, the satellite will have the opportunity to observe each of the five brightest stars in the sky with ten-minute average observation duration.
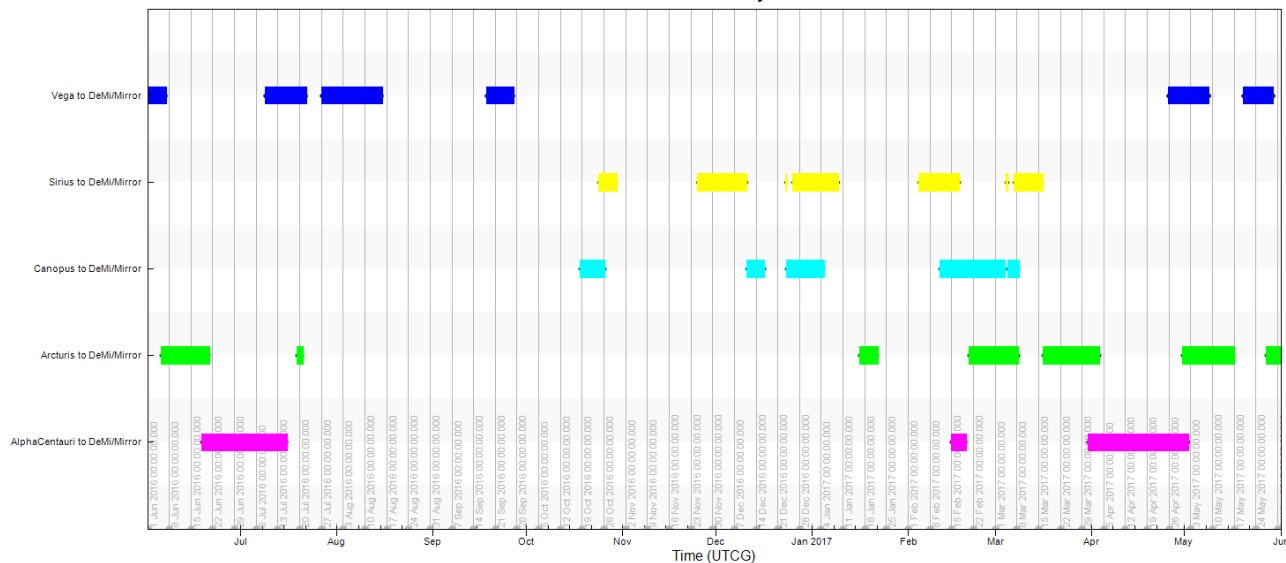

Figure 14: Occurrence of bright star observations for the baseline telescope field of view with maximum slew rate 0.1 degrees/s between June 1, 2016 and June 1, 2017

4.5 Spacecraft Jitter

In order for the satellite to take measurements and adequately correct the wavefront, the aberrations due to jitter must have minimal impact on the final image correction. To avoid complicated onboard or post-processing, the aberrations must have a small enough effect that the observed PSF is correctable. The effect of jitter can be minimized to a certain

extent by exposure time, but the shortest exposure time is limited by the physical limits of the detector frame readout. Figure 15 shows the effect of one-dimensional sinusoidal jitter on the PSF of an imaged star.
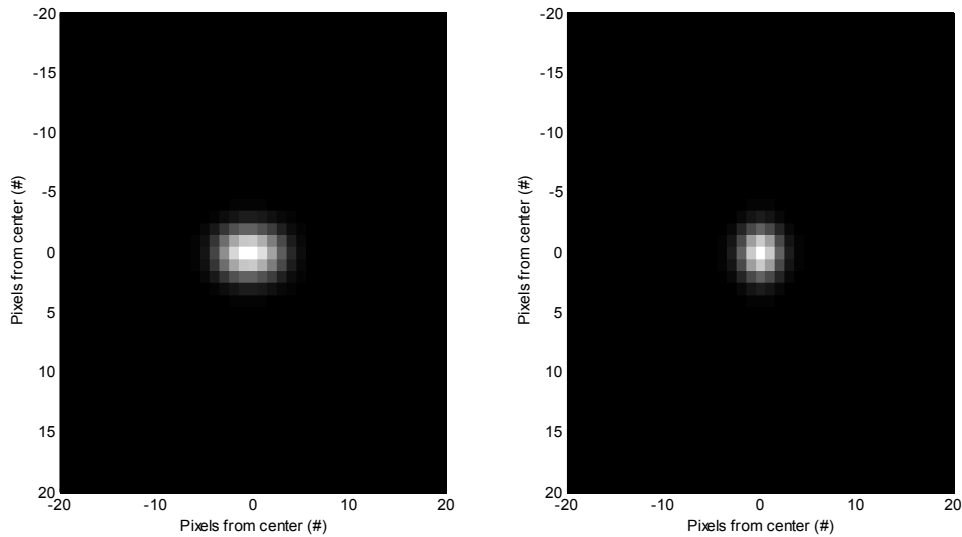

Figure 15: The effect of one-dimensional jitter (amplitude 9 as, frequency 92 Hz) (left) on a diffraction-limited PSF (right). Resulting Strehl: 0.61

To determine the susceptibility of the focal plane image to jitter, we simulated the effect of spacecraft jitter across a range of frequencies and magnitudes to determine how it impacts the Strehl number of the image. Figure 16 shows the resulting contours of Strehl number for the detector-limited exposure time of 0.019s. The system can withstand large-magnitude jitters with frequency less than about 2 Hz. Above this frequency, the system can withstand a jitter magnitude of up to 10 as without compromising image quality.
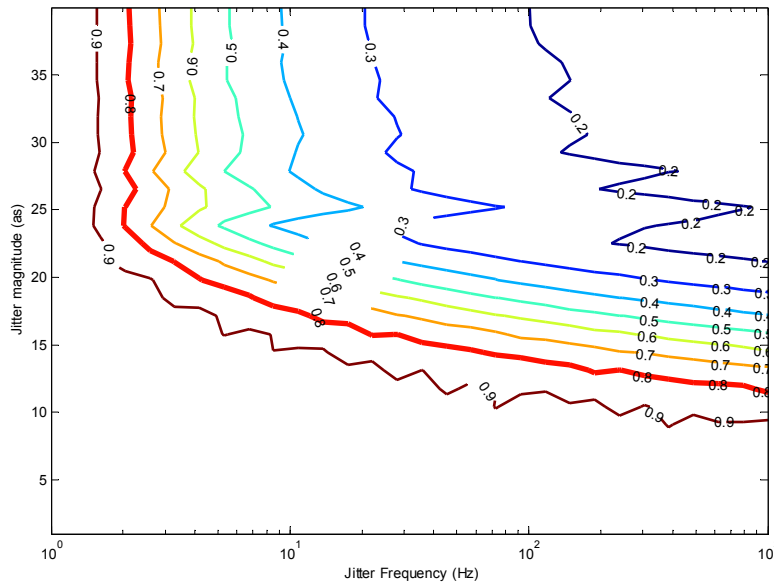

Figure 16: Contour plot of the effect of spacecraft jitter on the focal plane image quality for an exposure time of 0.019 s and a magnitude-0 star

Future work with this study involves extending the analysis to different jitter profiles and comparing the required performance to the state-of-the-art ADCS systems currently produced for CubeSats.

5. CONCLUSIONS

High-contrast imaging is a key capability for future space telescopes and requires the use of high-actuator-count MEMS deformable mirrors. Mirrors have gone through ground-based testing, but flight demonstration is required to fully understand and characterize the behavior of these devices in their intended operational environment. In this paper we presented the design, planned experiments, and preliminary simulations for the optical payload of a 3U CubeSat mission to characterize and demonstrate the operation of a MEMS deformable mirror in low-Earth orbit. The optical payload incorporates two types of sensors – a wavefront sensor with the mirror illuminated by an internal source, and a focal plane sensor for imaging bright stars – and fits within a 150 x 100 x 100 mm CubeSat-compatible volume and utilizes commercial off the shelf components wherever possible. The Shack-Hartmann wavefront sensor is designed to observe a maximum surface error of 11 µm with 6 nm resolution. The focal plane image sensor is a 12.5-mm aperture, 150-mm focal length telescope with the capability to detect stars brighter than magnitude 0.6. The telescope can accommodate jitter up to 10 as (larger magnitude at frequencies less than 2 Hz).

5.1 Future Work

Further steps in the development of the CubeSat optical payload include more detailed image modeling and hardware experimentations of the optical setup. The hardware setup will verify the feasibility of the optical design and provide a platform to validate the wavefront sensing algorithms. A virtual model of the end-to-end optical system will be used to optimize the payload layout and will be tied into spacecraft systems analyses on attitude determination and control, thermal, and structural designs.

ACKNOWLEDGEMENTS

REFERENCES

[1] Robert K. Tyson, Principles of Adaptive Optics. Boca Raton, FL, USA: CRC Press, 2011.

[2] B. R. Oppenheimer and S. Hinkley, "High-Contrast Observations in Optical and Infrared Astronomy," Annual Review of Astronomy & Astrophysics, vol. 47, no. 1, pp. 253-289, 2009.

[3] K. Stapelfeldt, "Extrasolar planets and star formation: science opportunities for future ELTs," The Scientific Requirements for Extremely Large Telescopes, Proceedings of the 232nd Symposium of the International Astronomical Union, pp. 149-158, November 2005.

[4] R. Angel, "Ground based imaging of extrasolar planets using adaptive optics," Nature, vol. 368, pp. 203-207, 1994.

[5] M. Perrin, A. Sivaramakrishnan, R. Makidon, B. Oppenheimer, and J. Graham, "The structure of high strehl ratio point-spread functions," Astrophysical Journal, vol. 596, pp. 702-712, 2003.

[6] B. Macintosh et al., "The Gemini Planet Imager: From science design to construction," in Proc. SPIE, pp. 7015-18.

[7] O. Guyon et al., "Exoplanet imaging with a Phase-induced Amplitude Apodization Coronagraph. I. Principle," Astrophysical Journal, vol. 622, pp. 744-758, 2005.

[8] Joseph Goodman, Introduction to Fourier Optics. Boston, MA: McGraw Hill, 1968.

[9] Sara Seager, Ed., Exoplanets. United States of America: The University of Arizona Press in collaboration with the Lunar and Planetary Institute, 2010.

[10] A. Sivaramakrishnan, J. Lloyd,. Hodge, and B. Macintosh, "Speckle decorrelation and dynamic range in speckle noise limited ranging," Astrophysical Journal, vol. 581, no. L59, pp. L59-L62, 2002.

[11] Ben Oppenheimer. (2008, March) The Lyot Project. Website. [Online]. http://www.lyot.org/results/

[12] Rus Belikov, "EXCEDE - Exoplanetary Circumstellar Environments and Disk Explorer," in ExoPAG 7, Long Beach, 2013.

[13] Erkin Sidick, Andreas Kuhnert, and John Trauger, "Broadband performance of TPF's High-Contrast imaging Testbed: Modeling and Simulations," in Proceedings of SPIE, vol. 6306-32, 2006.

[14] R. Belikov et al., "EXCEDE Techology Development I: First demonstrations of high contrast at 1.2 l/d for an Explorer space telescope mission," in Proc. of SPIE Vol. 8442 844209-5, 2012.

[15] John Trauger, "ACCESS - a science and engineering assessment of space coronagraph concepts for the direct imaging and spectroscopy of exoplanetary systems," in Beyond JWST Conference, Space Telescope Science Institute, 2009.

[16] Christopher Mendillo et al., "PICTURE: a sounding rocket experiment for direct imaging of an extrasolar planetary enviroment," in Proc. of SPIE, 2012.

[17] B. Yoo et al., "MEMS micromirror characterizationin space environments," Optics Express, vol. 17, pp. 3370-3380, 2009.

[18] J. Lee et al., "A New Type of Space Telescope for Observation of Extreme Lightning Phenomena in the Upper Atmosphere," IEEE Transactions on Geoscience and Remote Sensing, vol. 50, no. 10, pp. 3941-3949, 2012.

[19] Alexander Kutyrev et al., "Programmable microshutter arrays for the JWST NIRSpec: optical performance," IEEE Journal of Selected Topics in Quantum Electronics, vol. 10, no. 3, pp. 652-661, 2004.

[20] Ruth Marlaire. (2008, October) NASA Tests Optics Concept in New Coronagraph Laboratory. NASA.gov. [Online]. http://www.nasa.gov/centers/ames/research/2008/coron_lab.html

[21] The CubeSat Program, Cal Poly SLO. (2014) CubeSat Design Specification, Rev. 13. [Online]. http://cubesat.org/images/developers/cds_rev13_final.pdf

[22] D. Krejci and D. Selva, "A Survey and Assessment of the Capabilities of CubeSats for Earth Observation," Acta Astronautica, vol. 74, pp. 50-68, 2012.

[23] Hank Heidt, Jordi Puig-Suari, Augustus Moore, Shinichi Nakasuka, and Robert Twiggs, "CubeSat: A New Generation of Picosatellite for Education and Industry Low-Cost Space Experimentation," in SSC00-V-5, Logan, UT, 2001.

[24] Maria-Mihaela Burlacu and Pascal Lorenz, "A survey of small satellites domain challenges, applications, and communications issues," ICaST: ICST's Global Community Magazine, 2010.

[25] Kirk Woellert, Pascale Ehrenfreund, Antonio Ricco, and Henry Hertzfeld, "CubeSats: Cost-effective science and technology platforms for emerging and developing nations," Advances in Space Research, vol. 47, pp. 663-684, 2011.

[26] J. Springmann, A. Sloboda, A. Klesh, M. Bennett, and J. Cutler, "The attitude determination system of the RAX satellite," Acta Astronautica, vol. 75, pp. 120-135, 2012.

[27] Christopher Pong et al., "Achieving high-precision pointing on ExoplanetSat: initial feasibility analysis," in Proc. SPIE, vol. 7731, 2010, p. 7731V, doi:10.1117/12.857992.

[28] Anne Marinan, Austin Nicholas, and Kerri Cahoy, "Ad Hoc CubeSat Constellations: Secondary Launch Coverage and Distribution," in IEEE Aerospace, Big Sky, MO, 2013.

[29] Bill Blackwell et al, "Nanosatellites for Earth Environmental Monitoring: the MicroMAS Project," in Proceedings of the AIAA/USU Conference on Small Satellites, Logan, UT, 2012.

[30] Xingtao Wu, Li Yao, and Haijiang Ou, "Novel hierarchically dimensioned deformable mirrors with integrated ASIC driver electronics," in *Proc. SPIE 8253, MEMS Adaptive Optics VI*, San Francisco, CA, 2012.

[31] Hardy, John W. *Adaptive Optics for Astronomical Telescopes*. Oxford: Oxford University Press, 1998.